Geochemical Perspectives Letters

Hg isotopes constrain metallogenic effects of the Wilson Cycle of the Paleo-Asian Ocean

X. He[1], X. Deng[1*], M.J. Brzozowski[1], Y. Wu[2], J. Zhang[4], C. Wu[1], Y. Chen[2,5], R. Yin[3*]

OPEN ACCESS
https://doi.org/10.7185/geochemlet.2516

Abstract

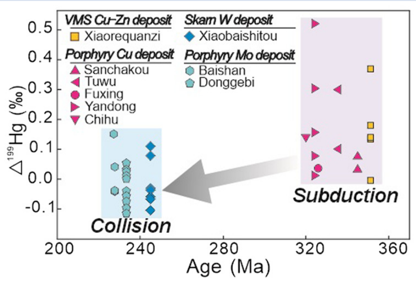

The Central Asian Orogenic Belt (CAOB) hosts a variety of hydrothermal mineralised systems that formed during the opening, development and closure of the Paleo-Asian Ocean. Mercury is an important ore-forming metal in hydrothermal systems. Mercury photoreactions on the surface of Earth produce negative and positive Δ^{199}Hg signals in terrestrial and marine sediments, respectively. Here, we observe positive Δ^{199}Hg values in 345 to 320 Ma porphyry Cu deposits (+0.15 ± 0.15 ‰, s.d.), and a 355 Ma volcanogenic massive sulfide Cu–Zn deposit (+0.16 ± 0.13 ‰, s.d.) in the CAOB, which reflect the recycling of marine sediments during oceanic subduction and circulation of seawater in an extensional tectonic regime, respectively. In contrast, we observe negative Δ^{199}Hg values in 232 to 227 Ma porphyry Mo deposits (−0.01 ± 0.07 ‰, s.d.) and a 245 Ma skarn W deposit (−0.02 ± 0.08 ‰, s.d.), which reflect the mixing of recycled Hg from marine and terrestrial sediments during continental collision. This study is useful in understanding the metallogenic effects of the Wilson Cycle and highlights that plate tectonics can cause intensive mobilisation, migration and mineralisation of Hg from subducted oceanic and continental crust to form Hg-bearing hydrothermal systems in long lived accretionary orogens.

Received 22 January 2025 | Accepted 14 April 2025 | Published 20 May 2025

Introduction

The Central Asian Orogenic Belt (CAOB), known as the world's largest Phanerozoic continental accretionary orogen (Şengör *et al.*, 1993), hosts a variety of hydrothermal mineralised systems, including porphyry Cu deposits, volcanogenic massive sulfide Cu–Zn deposits, porphyry Mo deposits, and skarn W deposits (Pirajno *et al.*, 2011). These hydrothermal systems formed in response to the Wilson Cycle (*i.e.* opening, development and closure) of the Paleo-Asian Ocean. In the early to middle stages of the Wilson Cycle, Paleo-Asian Ocean subduction and associated accretionary orogeny led to the occurrence of porphyry Cu deposits and volcanogenic massive sulfide Cu–Zn deposits between 355 to 320 Ma in the Eastern Tianshan segment of the CAOB (Mao *et al.*, 2020; Wang *et al.*, 2021). In the late stage of the Wilson Cycle, continental collision following closure of the Paleo-Asian Ocean led to the formation of porphyry Mo deposits and skarn W deposits between 245 and 227 Ma in the Eastern Tianshan segment of the CAOB (Deng *et al.*, 2017; Wu *et al.*, 2017). The diverse hydrothermal systems in the CAOB reflect the metallogenic effects of the Wilson Cycle.

Mercury (Hg) is an important ore-forming metal in hydrothermal systems. Hg isotopes display unique mass-dependent fractionation (MDF, δ^{202}Hg) and mass-independent fractionation (MIF, Δ^{199}Hg) (Blum and Berquist, 2007). MDF of Hg isotopes can occur during a large number of geochemical processes (*e.g.*, Blum *et al.*, 2014). However, MIF of Hg isotopes is predominantly associated with photoreactions in the land–ocean–atmosphere systems (Blum and Berquist, 2007). Hg(II) photoreduction has resulted in positive Δ^{199}Hg values in marine sediments and negative Δ^{199}Hg values in terrestrial sediments (Blum *et al.*, 2014). The primitive mantle displays near zero Δ^{199}Hg values (Moynier *et al.*, 2021). Considering that mineralogical and petrological processes cannot generate MIF of Hg isotopes, the unique Δ^{199}Hg signals across marine, terrestrial and mantle reservoirs allow for identification of the source of Hg and, by extension, other metals in hydrothermal systems (Yin *et al.*, 2022, 2024). Non-zero Δ^{199}Hg values have been detected in hydrothermal systems across diverse environments, demonstrating the recycling of terrestrial- or marine-derived Hg through oceanic subduction and continental collision (*e.g.*, Yin *et al.*, 2024).

This study presents the Hg isotope compositions of five porphyry Cu deposits, two porphyry Mo deposits, one volcanogenic massive sulfide Cu–Zn deposit, and one skarn W deposit in the Eastern Tianshan segment of the CAOB to clarify the metallogenic impacts of the Wilson Cycle. We demonstrate a large variation of Δ^{199}Hg in these deposits (−0.11 to +0.51 ‰), which reflects the recycling of marine- and terrestrial-derived Hg related to oceanic subduction and continental collision, respectively. During the Wilson Cycle, plate subduction contributed to mobilisation of

1. School of Earth Science and Resources, Chang'an University, Xi'an 710054, China
2. Xinjiang Research Center for Mineral Resources, Xinjiang Institute of Ecology and Geography, Chinese Academy of Sciences, Urumqi 830011, China
3. State Key Laboratory for Critical Mineral Research and Exploration, Institute of Geochemistry, Chinese Academy of Sciences, Guiyang 550081, China
4. State Key Laboratory of Geological Processes and Mineral Resources, China University of Geosciences, Beijing 100083, China
5. School of Earth and Space Science, Peking University, Beijing 100871, China
* Corresponding authors: Xiaohua Deng; Runsheng Yin (email: dxh198411@126.com; yinrunsheng@mail.gyig.ac.cn)

Hg from subducted oceanic and continental crusts to form various Hg-bearing hydrothermal systems in the accretionary orogen.

Geological Background

The CAOB is situated between the Siberian Craton to the north, Tarim and North China cratons to the south, and the East European Craton to the west (Fig. 1a; Jahn, 2004). The Eastern Tianshan metallogenic belt along the southern CAOB comprises the Harlik Belt, the Jueluotage Belt and the Central Tianshan Block, which are bound by the Kalamaili and Aqikekuduke faults (Fig. 1b; Qin *et al.*, 2002; Chen *et al.*, 2012). From north to south, the Jueluotage Belt is divided into the Dananhu-Tousuquan Arc, the Kangguer-Huangshan Shear Zone and the Aqishan-Yamansu Arc, by the Kangguer and Yamansu faults (Fig. 1c).

In the Carboniferous, double-sided subduction of the North Tianshan Ocean (NTO) formed the Dananhu-Tousuquan Arc and Aqishan-Yamansu Arc (Wang *et al.*, 2015). As shown in Figure 1c, the Dananhu-Tousuquan Arc contains numerous 355 to 320 Ma porphyry Cu deposits (*e.g.*, Tuwu, Yandong, Sanchakou, Fuxing and Chihu; Wang *et al.*, 2021; He *et al.*, 2023) and ~355 Ma volcanogenic massive sulfide Cu–Zn deposits (*e.g.*, Xiaorequanzi; He *et al.*, 2020; Mao *et al.*, 2020). The Aqishan-Yamansu Arc includes numerous 330–300 Ma volcanic-hosted Fe deposits (*e.g.*, Yamansu; Huang *et al.*, 2018). The NTO closed during the Triassic, resulting in the collision of the Dananhu-Tousuquan Arc and Aqishan-Yamansu Arc (Xiao *et al.*, 2004; Mao *et al.*, 2022). This collision formed the Kangguer-Huangshan Shear Zone and numerous 232 to 227 Ma porphyry Mo deposits (*e.g.*, Baishan and Donggebi; Wu *et al.*, 2017). The main deposit in the Central Tianshan Block is the 245 Ma Xiaobaishitou skarn-type W deposit (Deng *et al.*, 2017).

Methods

In this work, 14 granite rocks and 23 sulfide ores were collected from 5 porphyry Cu deposits (Tuwu, Yandong, Sanchakou, Fuxing and Chihu), 1 volcanogenic massive sulfide Cu–Zn deposit (Xiaorequanzi), 2 porphyry Mo deposits (Baishan and Donggebi), and 1 skarn-type W deposit (Xiaobaishitou) in the Eastern Tianshan. The geological characteristics of these ore deposits are summarised in Table 1. The comprehensive details of the samples are provided in Supplementary Information Table S-1.

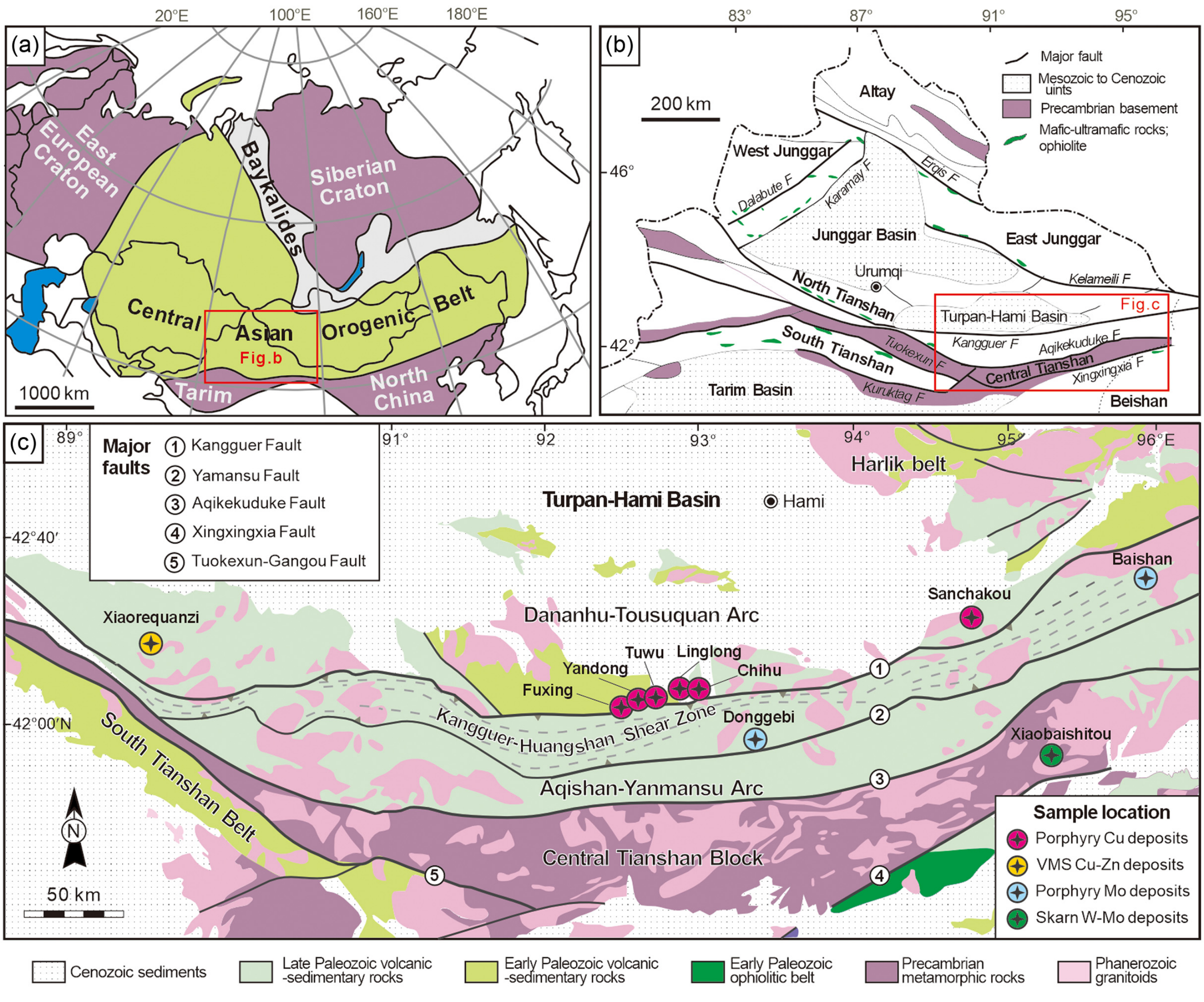

Figure 1 **(a)** Schematic map illustrating the precise location of the CAOB and the adjacent cratons (after Şengör *et al.*, 1993). **(b)** Geological map showing the emplacement of tectonic sections in the southern area of the CAOB (after Chen *et al.*, 2012). **(c)** Geological map exhibiting the arrangement of ore deposits in the Eastern Tianshan (after Wang *et al.*, 2006; Deng *et al.*, 2016).

Table 1 Description of the ore deposits studied in the Eastern Tianshan.

Location	Longitude (E°)	Latitude (N°)	Lithology	Tonnage and grade	Deposit type	Age of the granitoids (Ma)		Mineralisation age (Ma)
						Zircon U-Pb SHRIMP or SIMS	Zircon U-Pb LA-ICP-MS	Molybdenite Re-Os age (Ma)
Xiaorequanzi	89.53	42.29	Tuff	a combined measured reserve of 0.176 Mt Cu, 0.195 Mt Zn	volcanogenic massive sulfide Cu–Zn deposit	Tuff: 352 ± 5		354 ± 11
Sanchakou	94.76	42.39	Quartz diorite	0.5 Mt Cu with an average grade exceeding 0.5 % Cu	porphyry Cu deposit	Quartz diorite: 436 ± 11	Quartz diorite: 440 ± 3	345 ± 5
Tuwu	92.61	42.13	Plagiogranite porphyry	145 Mt Cu with a grade of 0.62 % Cu	porphyry Cu deposit	Plagiogranite porphyry: 334 ± 3	Plagiogranite porphyry: 356 ± 8	335 ± 2
Fuxing	92.33	42.08	Plagiogranite porphyry	Prospect	porphyry Cu deposit	Plagiogranite porphyry: 332 ± 2		
Yandong	92.53	42.1	Plagiogranite porphyry and quartz albite porphyry	372 Mt @ 0.58 % Cu	porphyry Cu deposit	Plagiogranite porphyry: 332 ± 2	Plagiogranite porphyry: 339 ±2 Quartz albite porphyry: 325 ± 2	325 ± 2
Chihu	93.03	42.17	Plagiogranite porphyry	Prospect	porphyry Cu deposit	Plagiogranite porphyry: 322 ± 10		316 ± 2
Xiaobaishitou	95.17	41.53	Biotite granite	36264 t W at an average grade of 0.78 % WO_3	skarn-type W deposit	-	Biotite granite: 242 ± 2	245 ± 4
Donggebi	93.38	41.93	Porphyritic granite and granite porphyry	0.508 Mt Mo with an average grade of 0.115 % Mo	porphyry Mo deposit	Porphyritic granite: 236 ± 2	Porphyritic granite: 235 ± 3	232 ± 6
Baishan	95.55	42.31	Granite porphyry	0.72 Mt Mo with an average grade of 0.06 % Mo	porphyry Mo deposit	Granite porphyry: 228 ± 2	Granite porphyry: 230 ± 1	227 ± 3

*Information for porphyry Cu deposits are from He *et al.* (2023) and references therein, for porphyry Mo deposits from Wu *et al.* (2017) and references therein, for the skarn-type W deposit from Deng *et al.* (2017), and for the volcanogenic massive sulfide Cu–Zn deposit from He *et al.* (2020) and Mao *et al.* (2020).

Analyses of Hg concentration and isotopic composition of the samples were done at the Institute of Geochemistry, Chinese Academy of Sciences. Comprehensive analytical methodologies are provided in Supplementary Information Text S-1. Hg-MDF is denoted in δ^{202}Hg in parts per thousand (‰), referring to the NIST-3133 Hg standard, which is examined prior and subsequent to each sample:

$$\delta^{202}\text{Hg}\ (‰) = [(^{202}\text{Hg}/^{198}\text{Hg}_{\text{sample}})/(^{202}\text{Hg}/^{198}\text{Hg}_{\text{standard}}) - 1] \times 1000 \quad \text{Eq. 1}$$

Hg-MIF is expressed as Δ, expressing the discrepancies between the observed and anticipated δ^{xxx}Hg values, where xxx = 199, 200 or 201, measured in per mil (‰):

$$\Delta^{xxx}\text{Hg} = \delta^{xxx}\text{Hg} - \delta^{202}\text{Hg} \times \beta \quad \text{Eq. 2}$$

β is 0.252 for ^{199}Hg, 0.5024 for ^{200}Hg and 0.752 for ^{201}Hg (Blum and Bergquist, 2007).

Results

The results of all samples are presented in Supplementary Information Table S-2. The Hg concentration varies largely among porphyry Cu deposits (granite porphyry: 4.90 to 27.9 ng/g; sulfides: 0.85 to 7860 ng/g), porphyry Mo deposits (porphyritic granite: 1.20 to 27.6 ng/g; sulfides: 38.3 to 143 ng/g), volcanogenic massive sulfide Cu–Zn deposit (sulfides: 315 to 8990 ng/g), and skarn-type W deposit (biotite granite: 4.30 to 33.9 ng/g; sulfides: 199 to 359 ng/g). The δ^{202}Hg values vary significantly among all samples (−3.14 to +1.29 ‰), although there is no systematic difference among the different deposit types (porphyry Cu deposits: −0.56 ± 0.96 ‰; porphyry Mo deposits: −0.78 ± 0.87 ‰; volcanogenic massive sulfide Cu–Zn deposit: −1.25 ± 1.18 ‰; skarn-type W deposit: −0.70 ± 1.03 ‰; average ± 1σ). A positive association variation trend exists between Δ^{201}Hg and Δ^{199}Hg values (Fig. 2a), aligning with the patterns observed in the land–ocean–atmosphere systems (Blum *et al.*, 2014). Based on Δ^{199}Hg values (−0.11 to +0.51 ‰), the samples can be categorised into two groups (Fig. 2b). The first group comprises porphyry Cu deposits and the volcanogenic massive sulfide Cu–Zn deposit, which exhibit positive Δ^{199}Hg values (+0.15 ± 0.15 ‰ and +0.16 ± 0.13 ‰, respectively) that are within the range of marine sediments. The second group comprises porphyry Mo deposits and the skarn-type W deposit, which exhibit near zero Δ^{199}Hg values (−0.01 ± 0.07 ‰ and −0.02 ± 0.08 ‰, respectively) that are intermediate to that of marine and terrestrial sediments.

Discussion

Recycling of marine sediments and seawater contributed subduction-related hydrothermal systems. Because MIF of Hg isotopes is mainly related to photochemical processes and does not occur during hydrothermal processes (Yin *et al.*, 2024), we utilise Δ^{199}Hg to analyse the origin of Hg and, by extension, other ore-forming metals in the investigated deposits. Sulfide samples from the studied porphyry Cu deposits and volcanogenic massive sulfide Cu–Zn deposit exhibit positive Δ^{199}Hg values (Fig. 2a, b; Δ^{199}Hg: +0.16 ‰ ± 0.14 ‰) that are similar to those of marine reservoirs (Fig. 2a; Blum *et al.*, 2014). The positive Δ^{199}Hg values of porphyry Cu deposits suggest that Hg originated from recycled marine materials. This is consistent with double-sided subduction of the NTO slab below the Dananhu-Tousuquan Arc and Aqishan-Yamansu Arc between 355 and 320 Ma (Fig. 3a; Jahn, 2004; Wang *et al.*, 2015). Analogous to this interpretation, volcanic arc-associated epithermal Au deposits formed in the circum-Pacific zone display mainly positive Δ^{199}Hg values (−0.02 to +0.27 ‰) due to the recycling of marine Hg from the subducted oceanic slab (Deng *et al.*, 2021). The exsolution of fluids from descending oceanic plates has been shown to play a key role in generating porphyry Cu and epithermal Au deposits in volcanic arcs (Richards, 2003). The positive Δ^{199}Hg values of marine sediments are likely to be inherited by these fluids released via slab dehydration (Deng *et al.*, 2021). The positive Δ^{199}Hg values of volcanogenic massive sulfide deposits can be explained by seawater circulation in an extensional tectonic regime induced by asthenospheric heat, since seawater contains Hg with positive Δ^{199}Hg values (Zhu *et al.*, 2020).

Recycling of terrestrial sediments contributed to collision-related hydrothermal systems. The near zero Δ^{199}Hg values in porphyry Mo deposits (−0.01 ± 0.07 ‰) and skarn-type W deposits (−0.02 ± 0.08 ‰) are intermediate to those of marine and terrestrial sediments (Fig. 2a). Terrestrial sediments are mainly characterised by negative Δ^{199}Hg values, whereas marine sediments mainly display positive Δ^{199}Hg values. The overall

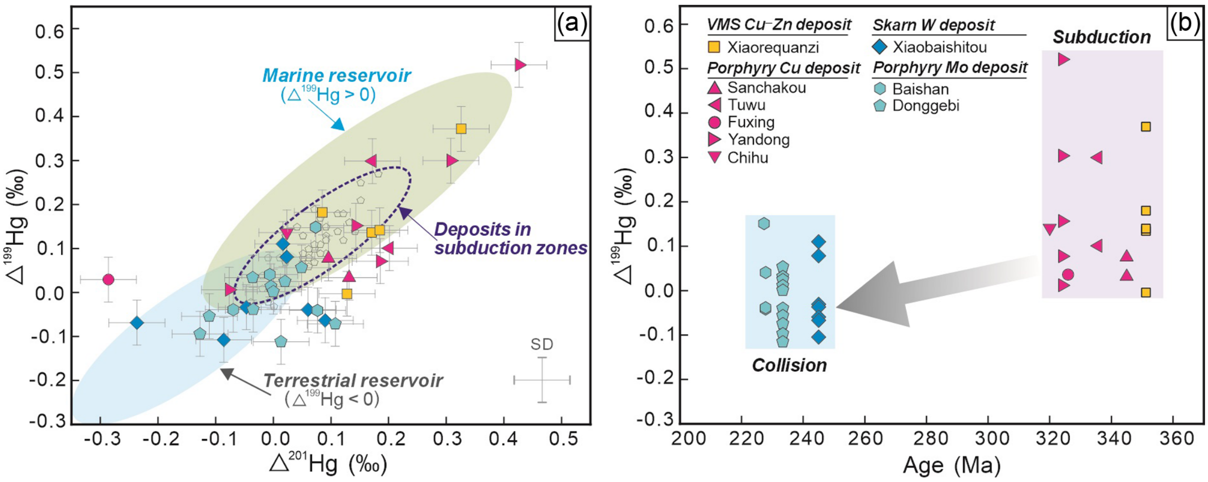

Figure 2 Binary diagrams displaying the variations in **(a)** Δ^{199}Hg–Δ^{201}Hg and **(b)** Δ^{199}Hg–Age (Ma) of the analysed ore deposits in the Eastern Tianshan. The area of marine sediments is delineated by Yin *et al.* (2015) and Meng *et al.* (2019), terrestrial sediments are characterised by Blum *et al.* (2014) and references therein, and subduction-related deposits are detailed by Deng *et al.* (2021).

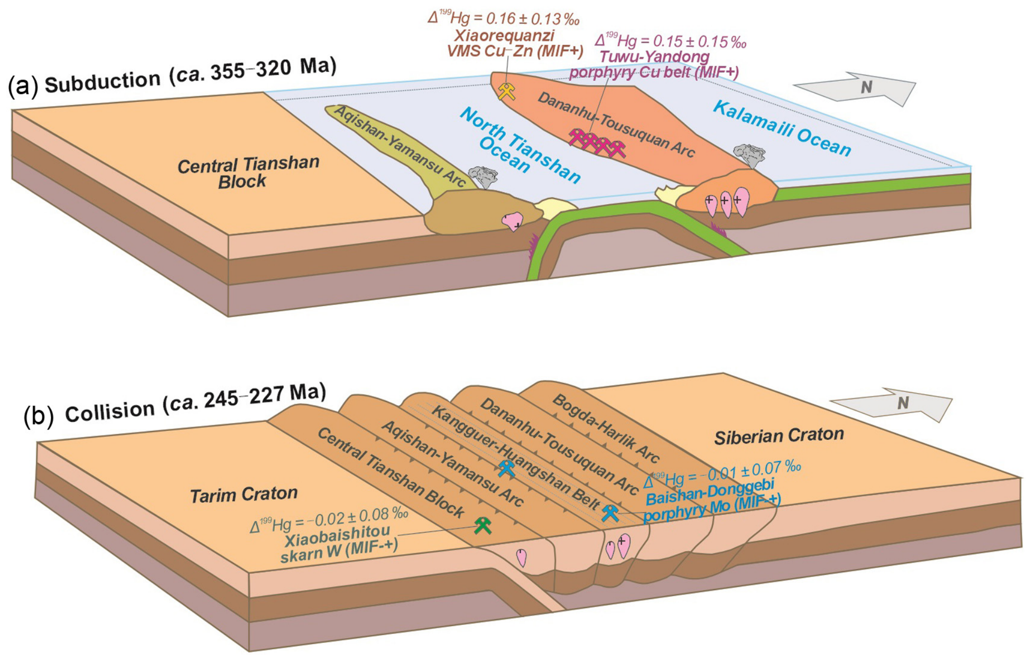

Figure 3 Schematic diagram illustrating the tectonic evolution of the Eastern Tianshan. **(a)** In the Carboniferous, the double-sided subduction of the NTO plate resulted in the formation of the Dananhu-Tousuquan Arc and Aqishan-Yamansu Arc, during which porphyry Cu deposits and volcanogenic massive sulfide Cu–Zn deposits were generated. **(b)** During the Triassic, the collision between the Tarim Craton and the Siberian Craton led to the formation of porphyry Mo deposits and skarn-type W deposits.

near zero Δ^{199}Hg values of the porphyry Mo deposits and skarn-type W deposit, with a few positive outliers, suggest contributions of Hg from both recycled marine sediments and terrestrial sediments during their formation. This interpretation is consistent with the relatively high $^{87}Sr/^{86}Sr_i$ values (0.7060 to 0.7088) of ore-bearing rocks coeval with porphyry Mo deposits and skarn-type W deposits in the Eastern Tianshan, which imply that oceanic subduction fertilised the mantle lithosphere (Deng *et al.*, 2017; Wu *et al.*, 2017). Continental subduction during the collisional stage would not only have released hydrothermal fluids with negative Δ^{199}Hg values, but also have caused partial melting and devolatilisation of metasomatised lithospheric mantle, releasing hydrothermal fluids with positive Δ^{199}Hg values (Deng *et al.*, 2022). Mercury in these two types of fluids tends to mix during upwards transport, and precipitate in tectonic weak zones. The negative Δ^{199}Hg values observed in the biotite granite of porphyry Mo deposits and skarn-type W deposits can be attributed to the closure of the NTO around *ca*. 245 Ma, and support the presence of continental arc magmatism in a collisional setting (Fig. 3b; Wu *et al.*, 2017).

Implications for the metallogenic effects of Wilson Cycles. The CAOB originated from long lived subduction, development and closure of the Paleo-Asian Ocean, during which the accretion of juvenile crust played a significant role in Phanerozoic continental growth (*e.g.*, Jahn, 2004; Xiao *et al.*, 2004, 2018). The observation of positive Δ^{199}Hg values in oceanic subduction-related hydrothermal systems (porphyry Cu deposits, volcanogenic massive sulfide Cu–Zn deposits), and near zero Δ^{199}Hg values in continental collision-related hydrothermal systems (porphyry Mo deposits, skarn-type W deposits) suggest that Hg from both continental and oceanic crusts can be remobilised by magmatic–hydrothermal fluids and concentrated to form Hg-bearing hydrothermal deposits at convergent plate margins. As shown in Figure 3, mobilisation of Hg via dehydration of subducted oceanic and continental slabs not only releases Hg-bearing hydrothermal fluids, but also transfers substantial quantities of Hg into the overlying mantle wedge, resulting in non-zero Δ^{199}Hg in the metasomatised lithospheric mantle. Partial melting and devolatilisation of the metasomatised lithospheric mantle, triggered by plate subduction, can also contribute metals for the generation of hydrothermal deposits in accretionary orogens.

Conclusions

Based on the newly generated Hg isotope dataset for magmatic-hydrothermal deposits in the Eastern Tianshan, this work demonstrates that oceanic subduction and continental collision can drive large scale recycling of Hg from oceanic and continental reservoirs into various hydrothermal systems within long lived accretionary orogens. In oceanic subduction-related porphyry Cu and volcanogenic massive sulfide Cu–Zn hydrothermal systems, the consistently positive Δ^{199}Hg values in sulfides indicate the dominant contribution of Hg from subducted marine sediments and circulated seawater, respectively. In continental collision-related hydrothermal systems (porphyry Mo deposits and skarn-type W deposits), the near zero Δ^{199}Hg values in sulfides suggest the contribution of Hg from subducted terrestrial sediments and the oceanic subduction fertilised mantle lithosphere. Overall, this work provides key knowledge into crust–mantle cycling of Hg and the metallogenic effects of oceanic subduction and continental collision during Wilson Cycles.

Acknowledgements

The research was supported by the Natural Science Foundation of China (42222205, 42430804, 41872084), National Key Research and Development Program of China (2018YFC0604006), Xinjiang Key Research and Development Project (2023B03015), and the Third Xinjiang Scientific Expedition Program (2022xjkk1301).

Editor: Horst Marschall

Additional Information

Supplementary Information accompanies this letter at https://www.geochemicalperspectivesletters.org/article2516.

Cite this letter as: He, X., Deng, X., Brzozowski, M.J., Wu, Y., Zhang, J., Wu, C., Chen, Y., Yin, R. (2025) Hg isotopes constrain metallogenic effects of the Wilson Cycle of the Paleo-Asian Ocean. *Geochem. Persp. Let.* 35, 7–12. https://doi.org/10.7185/geochemlet.2516

References

Blum, J.D., Bergquist, B.A. (2007) Reporting of variations in the natural isotopic composition of mercury. *Analytical and Bioanalytical Chemistry* 388, 353–359. https://doi.org/10.1007/s00216-007-1236-9.

Blum, J.D., Sherman, L.S., Johnson, M.W. (2014) Mercury isotopes in Earth and environmental sciences. *Annual Review of Earth and Planetary Sciences* 42, 249–269. https://doi.org/10.1146/annurev-earth-050212-124107.

Chen, Y.J., Pirajno, F., Wu, G., Qi, J.P., Xiong, X.L. (2012) Epithermal deposits in North Xinjiang, NW China. *International Journal of Earth Sciences* 101, 889–917. https://doi.org/10.1007/s00531-011-0689-4.

Deng, C.Z., Sun, G.Y., Rong, Y.M., Sun, R.Y., Sun, D.Y., Lehmann, B., Yin, R.S. (2021) Recycling of mercury from the atmosphere-ocean system into volcanic-arc–associated epithermal gold systems. *Geology* 49, 309–313. https://doi.org/10.1130/G48132.1.

Deng, C.Z., Gou, J., Sun, D.Y., Sun, G.Y., Tian, Z.D., Lehmann, B., Moynier, F., Yin, R.S. (2022) Mercury isotopic composition of igneous rocks from an accretionary orogen: Implications for lithospheric recycling. *Geology* 50, 1001–1006. https://doi.org/10.1130/G50131.1.

Deng, X.H., Wang, J.B., Pirajno, F., Wang, Y.W., Li, Y.C., Li, C., Zhou, L.M., Chen, Y.J. (2016) Re–Os dating of chalcopyrite from selected mineral deposits in the Kalatag district in the eastern Tianshan Orogen, China. *Ore Geology Reviews* 77, 72–81. https://doi.org/10.1016/j.oregeorev.2016.01.014.

Deng, X.H., Chen, Y.J., Santosh, M., Wang, J.B., Li, C., Yue, S.W., Zheng, Z., Chen, H.J., Tang, H.S., Dong, L.H., Qu, X. (2017) U–Pb zircon, Re–Os molybdenite geochronology and Rb–Sr geochemistry from the Xiaobaishitou W (–Mo) deposit: Implications for Triassic tectonic setting in eastern Tianshan, NW China. *Ore Geology Reviews* 80, 332–351. https://doi.org/10.1016/j.oregeorev.2016.05.013.

He, X.H., Deng, X.H., Bagas, L., Zhang, J., Li, C., Zhang, W.D. (2020) Geology, geochronology, and fluid inclusion studies of the Xiaorequanzi volcanogenic massive sulphide Cu–Zn deposit in the East Tianshan Terrane, China. *Canadian Journal of Earth Sciences* 57, 1392–1410. https://doi.org/10.1139/cjes-2019-0067.

He, X.H., Zhang, J., Deng, X.H., Long, L.L., Chen, L., Yin, Y.J., Zhang, Z.C. (2023) Metallogeny and tectonic setting of Paleozoic porphyry copper deposits in the East Tianshan. *Acta Petrologica Sinica* 39, 293–316. https://doi.org/10.18654/1000-0569/2023.02.02.

Huang, X.W., Zhou, M.F., Beaudoin, G., Gao, J.F., Qi, L., Lyu, C. (2018) Origin of the volcanic-hosted Yamansu Fe deposit, Eastern Tianshan, NW China: constraints from pyrite Re-Os isotopes, stable isotopes, and in situ magnetite trace elements. *Mineralium Deposita* 53, 1039–1060. https://doi.org/10.1007/s00126-018-0794-4.

Jahn, B.M. (2004) The Central Asian Orogenic Belt and growth of the continental crust in the Phanerozoic. In: Malpas, J., Fletcher, C.J.N., Ali, J.R., Aitchison, J.C. (Eds.) *Aspects of the Tectonic Evolution of China,* Geological Society of London Special Publication 226, 73–100. https://doi.org/10.1144/GSL.SP.2004.226.01.05.

Mao, Q., Wang, J., Yu, M., Ao, S., Deng, X., Lü, X., Li, Y. (2020) Re-Os and U-Pb geochronology for the Xiaorequanzi VMS deposit in the Eastern Tianshan, NW China: Constraints on the timing of mineralization and stratigraphy. *Ore Geology Reviews* 122, 103473. https://doi.org/10.1016/j.oregeorev.2020.103473.

Mao, Q., Ao, S., Windley, B.F., Zhang, Z., Sang, M., Tan, Z., Wang, H., Li, R., Xiao, W., Pan, Z. (2022) Middle–Late Triassic southward-younging granitoids: Tectonic transition from subduction to collision in the Eastern Tianshan–Beishan Orogen, NW China. *GSA Bulletin* 134, 2206–2224. https://doi.org/10.1130/B36172.1.

Meng, M., Sun, R.Y., Liu, H.W., Yu, B., Yin, Y.G., Hu, L.G., Shi, J.B., Jiang, G.B. (2019) An integrated model for input and migration of mercury in Chinese coastal sediments. *Environmental Science and Technology* 53, 2460–2471. https://doi.org/10.1021/acs.est.8b06329.

Moynier, F., Jackson, M.G., Zhang, K., Cai, H.M., Halldórsson, S.A., Pik, R., Day, J.M.D., Chen, J.B. (2021) The mercury isotopic composition of Earth's mantle and the use of mass independently fractionated Hg to test for recycled crust. *Geophysical Research Letters* 48, e2021GL094301. https://doi.org/10.1029/2021GL094301.

Pirajno, F., Seltmann, R., Yang, Y.Q. (2011) A review of mineral systems and associated tectonic settings of northern Xinjiang, NW China. *Geoscience Frontiers* 2, 157–185. https://doi.org/10.1016/j.gsf.2011.03.006.

Qin, K.Z., Fang, T.H., Wang, S.L. (2002) Plate tectonics division, evolution and metallogenic settings in eastern Tianshan mountains, NW China. *Xinjiang Geology* 20, 302–308. (in Chinese with English abstract)

Richards, J.P. (2003) Tectono-magmatic precursors for porphyry Cu-(Mo-Au) deposit formation. *Economic Geology* 98, 1515–1533. https://doi.org/10.2113/gsecongeo.98.8.1515.

Şengör, A.M.C., Natal'in, B.A., Burtman, V.S. (1993) Evolution of the Altaid tectonic collage and Palaeozoic crustal growth in Eurasia. *Nature* 364, 299–307. https://doi.org/10.1038/364299a0.

Wang, J.B., Wang, Y.W., He, Z.H. (2006) Ore deposits as a guide to the tectonic evolution in the east Tianshan mountains, NW China. *Geology in China* 33, 461–469.

Wang, Y.H., Xue, C.J., Liu, J.J., Wang, J.P., Yang, J.T., Zhang, F.F., Zhao, Z.N., Zhao, Y.J., Liu, B. (2015) Early Carboniferous adakitic rocks in the area of the Tuwu deposit, eastern Tianshan, NW China: Slab melting and implications for porphyry copper mineralization. *Journal of Asian Earth Sciences* 103, 332–349. https://doi.org/10.1016/j.jseaes.2014.09.032.

Wang, Y.H., Zhang, F.F., Xue, C.J., Liu, J.J., Zhang, Z.C., Sun, M. (2021) Geology and Genesis of the Tuwu Porphyry Cu Deposit, Xinjiang, Northwest China. *Economic Geology* 116, 471–500. https://doi.org/10.5382/econgeo.4763.

Wu, Y.S., Chen, Y.J., Zhou, K.F. (2017) Mo deposits in Northwest China: Geology, geochemistry, geochronology and tectonic setting. *Ore Geology Reviews* 81, 641–671. https://doi.org/10.1016/j.oregeorev.2016.07.010.

Xiao, W.J., Zhang, L.C., Qin, K.Z., Sun, S., Li, J.L. (2004) Paleozoic accretionary and collisional tectonics of the eastern Tianshan (China): Implications for the continental growth of central Asia. *American Journal of Science* 304, 370–395. https://doi.org/10.2475/ajs.304.4.370.

Xiao, W.J., Windley, B.F., Han, C., Liu, W., Wan, B., Zhang, J.E., Ao, S., Zhang, Z., Song, D. (2018) Late Paleozoic to early Triassic multiple roll-back and oroclinal bending of the Mongolia collage in Central Asia. *Earth-Science Reviews* 186, 94–128. https://doi.org/10.1016/j.earscirev.2017.09.020.

Yin, R.S., Feng, X.B., Chen, B., Zhang, J., Wang, W., Li, X. (2015) Identifying the sources and processes of mercury in subtropical estuarine and ocean sediments using Hg isotopic composition. *Environmental Science and Technology* 49, 1347–1355. https://doi.org/10.1021/es504070y.

Yin, R.S., Chen, D., Pan, X., Deng, C.Z., Chen, L.M., Song, X.Y., Yu, S.Y., Zhu, C.W., Wei, X., Xu, Y., Feng, X.B., Blum, J.D., Lehmann, B. (2022) Mantle Hg isotopic heterogeneity and evidence of oceanic Hg recycling into the mantle. *Nature Communications* 13, 948. https://doi.org/10.1038/s41467-022-28577-1.

Yin, R.S., Wang, X., Sun, R., Gao, L., Deng, C., Tian, Z., Luo, A., Lehmann, B. (2024) Linking the mercury biogeochemical cycle to the deep mercury cycle: A mercury isotope perspective. *Chemical Geology* 654, 122063. https://doi.org/10.1016/j.chemgeo.2024.122063.

Zhu, C., Tao, C., Yin, R., Liao, S., Yang, W., Liu, J., Barriga, F.J.A.S. (2020) Seawater versus mantle sources of mercury in sulfide-rich seafloor hydrothermal systems, Southwest Indian Ridge. *Geochimica et Cosmochimica Acta* 281, 91–101. https://doi.org/10.1016/j.gca.2020.05.008.

Geochemical Perspectives Letters EAG

Hg isotopes constrain metallogenic effects of the Wilson Cycle of the Paleo-Asian Ocean

X. He, X. Deng, M.J. Brzozowski, Y. Wu, J. Zhang, C. Wu, Y. Chen, R. Yin

Supplementary Information

The Supplementary Information includes:

- Methods
- Tables S-1 to S-3
- Supplementary Information References

Methods

The samples were processed using a double-stage tube furnace coupled with 40% anti aqua regia (HNO_3/HCl = 3/1, v/v) trapping solutions (Zerkle *et al.*, 2020). The trapping solutions were measured using an F732 atomic absorption spectroscopy for the total Hg (THg) concentrations of the samples. Measurements of GSS-4 standard reference material yielded THg recoveries of 90-110% and uncertainty of < 10% for sample triplicates. The trapping solutions were diluted to 1 ng/mL Hg and measured by a Neptune Plus multi-collector inductively-coupled plasma mass spectrometer for Hg isotope ratios (Yin *et al.*, 2016). Hg-MDF is expressed in δ^{202}Hg notation in units of ‰ referenced to the NIST-3133 Hg standard (analyzed before and after each sample):

$$\delta^{202}\text{Hg}\ (‰) = [(^{202}\text{Hg}/^{198}\text{Hg}_{\text{sample}})/(^{202}\text{Hg}/^{198}\text{Hg}_{\text{standard}}) - 1] \times 1000 \quad (1)$$

MIF is reported in Δ notation, which describes the difference between the measured δ^{xxx}Hg and the theoretically predicted δ^{xxx}Hg value, in units of ‰:

$$\Delta^{xxx}\text{Hg} = \delta^{xxx}\text{Hg} - \delta^{202}\text{Hg} \times \beta \quad (2)$$

where β is 0.2520 for ^{199}Hg, 0.5024 for ^{200}Hg, and 0.7520 for ^{201}Hg. Analytical uncertainty was estimated based on the replication of the NIST-3177 standard solution. The average and uncertainty of NIST-3177 (δ^{202}Hg: -0.53 ± 0.06 ‰; Δ^{199}Hg: -0.01 ± 0.05 ‰; Δ^{200}Hg: 0.01 ± 0.04 ‰; Δ^{201}Hg: -0.02 ± 0.05 ‰, SD, n = 21) and GSS-4 (δ^{202}Hg: -1.63 ± 0.07 ‰; Δ^{199}Hg: -0.46 ± 0.04 ‰; Δ^{200}Hg: -0.02 ± 0.03 ‰; Δ^{201}Hg: -0.41± 0.05 ‰, SD, n = 7), agrees well with previous results. The larger SD values for NIST-3177 and GSS-4 represent the analytical uncertainties of our samples (see Table S-3 for the Hg isotope data of Standard reference material).

Supplementary Tables

Table S-1 Description of samples used in this study.

Sample	Location	Type	Longitude	Latitude	Age (Ma)	Mineral assemblage	Wall rock
Deposit in oceanic subduction zone							
XRQZ24-1	Xiaorequanzi Cu-Zn deposit	Chalcopyrite			355		
XRQZ24-2	Xiaorequanzi Cu-Zn deposit	Chalcopyrite			355		
XRQZ24-3	Xiaorequanzi Cu-Zn deposit	Sphalerite	89.53	42.30	355	Ccp+Py+Sp	Tuff
XRQZ24-4	Xiaorequanzi Cu-Zn deposit	Sphalerite			355		
XRQZ24-5	Xiaorequanzi Cu-Zn deposit	Chalcopyrite			355		
9SCK-37	Sanchakou Cu deposit	Chalcopyrite	94.76	42.40	345	Ccp+Py+Mag	Quartz diorite
9SCK63	Sanchakou Cu deposit	Chalcopyrite			345		
TWZK1507	Tuwu Cu deposit	Plagiogranite porphyry	92.61	42.10	335	Pl+Qz+Chl+Ep+Bt+ Ccp+Py+Mag+Mol	-
TWZK1507	Tuwu Cu deposit	Ore			335	Ccp+Py+Mag+Mol+ Qz+Chl+Ep+Bt	Plagiogranite porphyry
FX22-1	Fuxing Cu deposit	Plagiogranite porphyry	92.33	42.08	332	Pl+Qz+Bt+Ccp+Py+ Mag+Mol	-
YDZK008-297	Yandong Cu deposit	Quartz albite porphyry			325	Pl+Qz+Ab+Bt+Ccp+ Py+Mag+Mol	-
YD23-1	Yandong Cu deposit	Ore			325		
YD23-2	Yandong Cu deposit	Ore	92.53	42.10	325	Ccp+Py+Mag+Mol+ Qz+Ab+Chl+Ep+Bt	Quartz albite porphyry, plagiogranite porphyry
YD23-3	Yandong Cu deposit	Ore			325		
YD23-4	Yandong Cu deposit	Ore			325		
CH22-3	Chihu Cu deposit	Plagiogranite porphyry	93.03	42.17	322	Pl+Qz+Bt+Ccp+Py+ Mag+Mol	-
Deposit in collisional settings							
11bst-M21	Xiaobaishitou W deposit	Molybdenite	95.17	41.5	245	Qz+Sch+Mol+Py+Gr t+Cal	Limestone
11bst-M23	Xiaobaishitou W deposit	Molybdenite			245		

11bst-G2	Xiaobaishitou W deposit	Biotite granite			242		-
11bst-G5	Xiaobaishitou W deposit	Biotite granite			242		-
11bst-G7	Xiaobaishitou W deposit	Biotite granite			242	Pl+Kfs+Qz+Bt	-
11bst-G9	Xiaobaishitou W deposit	Biotite granite			242		-
11bst-G10	Xiaobaishitou W deposit	Biotite granite			242		-
ZK0312-3	Donggebi Mo deposit	Porphyritic granite			236		-
ZK0312-4	Donggebi Mo deposit	Porphyritic granite			236		-
ZK0106-1	Donggebi Mo deposit	Porphyritic granite			236	Pl+Kfs+Qz+Bt	-
ZK0312	Donggebi Mo deposit	Porphyritic granite			236		-
ZK0106-2	Donggebi Mo deposit	Porphyritic granite	93.38	41.9	236		-
ZK03-47	Donggebi Mo deposit	Molybdenite			232		
ZK0408-2	Donggebi Mo deposit	Molybdenite			232		
ZK0408-3	Donggebi Mo deposit	Molybdenite			232	Qz+Mol+Py+Ccp	Sandstone
ZK0408-6	Donggebi Mo deposit	Molybdenite			232		
ZK0408-7	Donggebi Mo deposit	Molybdenite			232		
BS0408	Baishan Mo deposit	Pyrite			227		
19BS	Baishan Mo deposit	Molybdenite			227		
19BS-2	Baishan Mo deposit	Molybdenite	95.55	42.3	227	Qz+Kfs+Mol+Py	tuff, basalt, and shale
19BS-1	Baishan Mo deposit	Pyrite			227		

*Ccp = chalcopyrite; Py = pyrite; Sp = sphalerite; Mag = magnetite; Sch = scheelite; Grt = garnet; Ab = albite; Bt = biotite; Pl = plagioclase; Qz = quartz; Kfs = K-feldspar; Cal = calcite

Table S-2 The Hg isotope data of subduction to collisional ore systems in the CAOB.

Sample	Location	Type	Deposit type	THg (ng/g)	δ^{199}Hg	δ^{200}Hg	δ^{201}Hg	δ^{202}Hg	Δ^{199}Hg	Δ^{200}Hg	Δ^{201}Hg
Deposit in oceanic subduction zone											
XRQZ 24-1	Xiaorequanzi Cu-Zn deposit	Chalcopyrite	Volcanogenic massive sulfide (VMS) Cu-Zn deposit	962.69	-0.14	-0.16	-0.26	-0.52	0.00	0.10	0.13
XRQZ 24-2	Xiaorequanzi Cu-Zn deposit	Chalcopyrite	Volcanogenic massive sulfide (VMS) Cu-Zn deposit	8988.43	0.15	-0.09	0.00	-0.11	0.18	-0.03	0.08
XRQZ 24-3	Xiaorequanzi Cu-Zn deposit	Sphalerite	Volcanogenic massive sulfide (VMS) Cu-Zn deposit	530.50	-0.42	-1.41	-2.04	-3.14	0.37	0.17	0.32
XRQZ 24-4	Xiaorequanzi Cu-Zn deposit	Sphalerite	Volcanogenic massive sulfide (VMS) Cu-Zn deposit	1046.80	-0.26	-0.79	-0.99	-1.55	0.13	-0.01	0.17
XRQZ 24-5	Xiaorequanzi Cu-Zn deposit	Chalcopyrite	Volcanogenic massive sulfide (VMS) Cu-Zn deposit	315.39	-0.10	-0.37	-0.54	-0.96	0.14	0.11	0.18
9SCK-37	Sanchakou Cu deposit	Chalcopyrite	Porphyry Cu deposit	129.31	-0.23	-0.57	-0.83	-1.23	0.08	0.05	0.10
9SCK63	Sanchakou Cu deposit	Chalcopyrite	Porphyry Cu deposit	0.85	-0.20	-0.51	-0.56	-0.92	0.03	-0.05	0.13
TWZK 1507	Tuwu Cu deposit	Plagiogranite porphyry	Porphyry Cu deposit	4.90	0.19	0.29	0.48	0.37	0.10	0.10	0.20
TWZK 1507	Tuwu Cu deposit	Ore	Porphyry Cu deposit	2485.21	0.62	0.70	1.14	1.29	0.30	0.05	0.17
FX22-1	Fuxing Cu deposit	Plagiogranite porphyry	Porphyry Cu deposit	27.90	-0.01	-0.26	-0.39	-0.14	0.03	-0.19	-0.28
YDZK 008-297	Yandong Cu deposit	Quartz albite porphyry	Porphyry Cu deposit	7.80	-0.10	-0.25	-0.32	-0.68	0.07	0.09	0.18
YD23-1	Yandong Cu deposit	Ore	Porphyry Cu deposit	836.07	0.00	-0.46	-0.58	-1.17	0.30	0.13	0.31
YD23-2	Yandong Cu deposit	Ore	Porphyry Cu deposit	278.43	0.05	-0.22	-0.16	-0.41	0.15	-0.01	0.14

YD23-3	Yandong Cu deposit	Ore	Porphyry Cu deposit	7855.67	0.07	-0.75	-0.90	-1.77	0.51	0.14	0.42
YD23-4	Yandong Cu deposit	Ore	Porphyry Cu deposit	176.33	0.08	0.11	0.13	0.28	0.00	-0.03	-0.08
CH22-3	Chihu Cu deposit	Plagiogranite porphyry	Porphyry Cu deposit	19.20	-0.32	-0.98	-1.34	-1.81	0.13	-0.07	0.02
<u>Deposit in collisional settings</u>											
11bst-M21	Xiaobaishitou W deposit	Molybdenite	Skarn W deposit	198.71	-0.46	-1.15	-1.69	-2.27	0.11	-0.01	0.02
11bst-M23	Xiaobaishitou W deposit	Molybdenite	Skarn W deposit	359.20	-0.44	-1.03	-1.51	-2.05	0.08	0.00	0.02
11bst-G2	Xiaobaishitou W deposit	Biotite granite	Skarn W deposit	20.70	-0.01	0.14	0.14	0.10	-0.04	0.09	0.06
11bst-G5	Xiaobaishitou W deposit	Biotite granite	Skarn W deposit	11.80	-0.02	0.06	-0.02	0.04	-0.03	0.04	-0.05
11bst-G7	Xiaobaishitou W deposit	Biotite granite	Skarn W deposit	4.30	-0.02	0.04	-0.10	0.18	-0.07	-0.05	-0.24
11bst-G9	Xiaobaishitou W deposit	Biotite granite	Skarn W deposit	10.30	-0.19	-0.19	-0.33	-0.33	-0.11	-0.03	-0.09
11bst-G10	Xiaobaishitou W deposit	Biotite granite	Skarn W deposit	33.90	-0.21	-0.16	-0.34	-0.57	-0.06	0.12	0.09
ZK0312-3	Donggebi Mo deposit	Porphyritic granite	Porphyry Mo deposit	1.20	-0.47	-0.82	-1.32	-1.71	-0.04	0.03	-0.03
ZK0312-4	Donggebi Mo deposit	Porphyritic granite	Porphyry Mo deposit	1.20	-0.47	-0.65	-1.07	-1.57	-0.07	0.13	0.11
ZK0106-1	Donggebi Mo deposit	Porphyritic granite	Porphyry Mo deposit	27.60	-0.12	-0.23	-0.36	-0.47	0.00	0.01	0.00
ZK0312	Donggebi Mo deposit	Porphyritic granite	Porphyry Mo deposit	19.00	-0.25	-0.39	-0.69	-0.78	-0.06	0.00	-0.11
ZK0106-2	Donggebi Mo deposit	Porphyritic granite	Porphyry Mo deposit	7.80	-0.16	-0.36	-0.61	-0.76	0.03	0.02	-0.04
ZK03-47	Donggebi Mo deposit	Molybdenite	Porphyry Mo deposit	114.94	-0.09	-0.19	-0.31	-0.44	0.02	0.03	0.02
ZK0408-2	Donggebi Mo deposit	Molybdenite	Porphyry Mo deposit	39.96	-0.34	-0.76	-1.12	-1.55	0.05	0.02	0.05
ZK0408-3	Donggebi Mo deposit	Molybdenite	Porphyry Mo deposit	68.97	-0.21	-0.18	-0.46	-0.44	-0.09	0.04	-0.13
ZK0408-6	Donggebi Mo deposit	Molybdenite	Porphyry Mo deposit	53.67	-0.27	-0.52	-0.84	-1.12	0.01	0.04	0.00
ZK0408-7	Donggebi Mo deposit	Molybdenite	Porphyry Mo deposit	38.31	-0.27	-0.23	-0.45	-0.62	-0.11	0.08	0.01
BS0408	Baishan Mo deposit	Pyrite	Porphyry Mo deposit	142.76	0.13	0.37	0.44	0.68	-0.04	0.03	-0.07
19BS	Baishan Mo deposit	Molybdenite	Porphyry Mo deposit	79.02	0.32	0.59	0.83	1.11	0.04	0.03	-0.01
19BS-2	Baishan Mo deposit	Molybdenite	Porphyry Mo deposit	46.42	-0.33	-0.89	-1.34	-1.89	0.15	0.06	0.08
19BS-1	Baishan Mo deposit	Pyrite	Porphyry Mo deposit	105.13	-0.38	-0.66	-0.92	-1.32	-0.04	0.00	0.08

Table S-3 Hg isotope data of standard reference materials used to calculate analytical uncertainty.

Sample	δ^{199}Hg	δ^{200}Hg	δ^{201}Hg	δ^{202}Hg	Δ^{199}Hg	Δ^{200}Hg	Δ^{201}Hg
GSS-4-1	-0.84	-0.87	-1.64	-1.61	-0.43	-0.06	-0.43
GSS-4-2	-0.88	-0.82	-1.57	-1.65	-0.46	0.01	-0.33
GSS-4-3	-0.92	-0.86	-1.75	-1.72	-0.49	0.00	-0.46
GSS-4-4	-0.85	-0.83	-1.65	-1.64	-0.43	-0.01	-0.42
GSS-4-5	-0.86	-0.91	-1.64	-1.68	-0.43	-0.06	-0.38
GSS-4-6	-0.92	-0.84	-1.64	-1.55	-0.53	-0.06	-0.47
GSS-4-7	-0.84	-0.76	-1.51	-1.54	-0.45	0.01	-0.35
NIST-3177-1	-0.20	-0.29	-0.39	-0.56	-0.06	-0.01	0.03
NIST-3177-2	-0.07	-0.20	-0.41	-0.56	0.07	0.08	0.01
NIST-3177-3	-0.19	-0.21	-0.34	-0.44	-0.08	0.01	-0.01
NIST-3177-4	-0.20	-0.26	-0.51	-0.56	-0.06	0.02	-0.09
NIST-3177-5	-0.03	-0.23	-0.39	-0.44	0.08	-0.01	-0.05
NIST-3177-6	-0.15	-0.23	-0.41	-0.50	-0.02	0.03	-0.03
NIST-3177-7	-0.16	-0.28	-0.43	-0.45	-0.05	-0.05	-0.08
NIST-3177-8	-0.14	-0.21	-0.38	-0.49	-0.01	0.04	-0.02
NIST-3177-9	-0.09	-0.21	-0.30	-0.44	0.02	0.01	0.03
NIST-3177-10	-0.07	-0.28	-0.49	-0.54	0.06	-0.01	-0.08
NIST-3177-11	-0.11	-0.26	-0.46	-0.56	0.03	0.02	-0.04
NIST-3177-12	-0.15	-0.24	-0.40	-0.59	0.00	0.06	0.05
NIST-3177-13	-0.21	-0.35	-0.50	-0.58	-0.07	-0.06	-0.07
NIST-3177-14	-0.19	-0.29	-0.45	-0.60	-0.04	0.01	0.01
NIST-3177-15	-0.07	-0.32	-0.46	-0.54	0.06	-0.05	-0.05
NIST-3177-16	-0.22	-0.30	-0.45	-0.67	-0.05	0.04	0.06
NIST-3177-17	-0.20	-0.26	-0.48	-0.56	-0.06	0.03	-0.06
NIST-3177-18	-0.12	-0.21	-0.36	-0.50	0.00	0.04	0.01
NIST-3177-19	-0.13	-0.24	-0.33	-0.53	0.00	0.02	0.07
NIST-3177-20	-0.18	-0.37	-0.52	-0.62	-0.02	-0.06	-0.05
NIST-3177-21	-0.19	-0.20	-0.36	-0.46	-0.07	0.03	-0.01

Supplementary Information References

Yin, R., Krabbenhoft, D.P., Bergquist, B.A., Zheng, W., Lepak, R.F., Hurley, J.P. (2016) Effects of mercury and thallium concentrations on high precision determination of mercury isotopic composition by Neptune Plus multiple collector inductively coupled plasma mass spectrometry. *Journal Of Analytical Atomic Spectrometry* 31, 2060-2068. https://doi.org/10.1039/C6JA00107F.

Zerkle, A.L., Yin, R., Chen, C., Li, X., Izon, G.J., Grasby, S.E. (2020) Anomalous fractionation of mercury isotopes in the Late Archean atmosphere. *Nature Communications* 11, 1709. https://doi.org/10.1038/s41467-020-15495-3